Bimodal, Thin Wick Structures for High Heat Flux Two-Phase Thermal Control Systems

Nathan Albu[1], Jacob Keese[2], Gisuk Hwang[3]

Wichita State University, Wichita, KS, 67260

Modern electronic devices and power conversion systems in space technologies dissipate large amounts of heat through small surface areas, requiring advanced thermal control systems with high heat flux thermal management capabilities. Two-phase thermal control systems, i.e. heat pipes and vapor chambers, offer high heat flux cooling capabilities with reliable operations, and thin wick structures improve their cooling capabilities by assisting liquid supply to the heated surface, thereby avoiding premature surface dryout. Premature surface dryout is related to wicking ability, but it is primarily understood for wick structures with uniform particle-size distribution. The objective of this study is to explore and quantify the enhanced wicking ability of wick structures with bimodal particle-size distributions. This study examines the hypothesis that utilizing bimodal particle sizes in single-layer and multi-layer wick structures improves the wicking ability by creating extra liquid-permeable space from larger particle sizes and decreasing the effective pore radius from smaller particle sizes. The wick structures are manufactured using a sintering process with spherical copper particles ranging from 100-200 μm in diameter. To measure wicking ability, the rate-of-rise test is used. One end of the sample is submerged in liquid acetone, causing the liquid to rise upward into the wick due to capillary suction. The rising liquid front is recorded with a video camera and the resulting video data is processed to analyze the wicking ability and calculate properties such as permeability and effective pore radius. The experimental results show that the wicking ability of the thin bimodal wick structures is significantly higher than that of thin wick structures with uniform particle-size distribution. This knowledge will provide an insight into optimal designs of advanced thermal management systems by discovering the relationship between particle size distributions and wicking ability.

Nomenclature

d_p	particle diameter, m
ε	porosity
h	wetted height, m
h_{eq}	equilibrium height, m
K	permeability, m^2
μ	viscosity, m^2/s
ρ	density, kg/m^3
θ	contact angle, degrees
r_{eff}	effective pore radius, m
σ	surface tension, N/m

[1] Undergraduate Student, Department of Mechanical Engineering, 1845 Fairmount St., Wichita, MB101.
[2] Undergraduate Student, Department of Mechanical Engineering, 1845 Fairmount St., Wichita, MB101.
[3] Assistant Professor, Department of Mechanical Engineering, 1845 Fairmount St., Wichita, MB101.

I. Introduction

An effective thermal control system is critical to prevent temperatures from exceeding the allowable range and causing damage to spacecraft. Two-phase thermal control systems, i.e., heat pipes and vapor chambers, offer reliable high heat flux cooling capability[1,2]. However, the maximum heat flux is limited by coolant supply to the heated surface, which can be increased by improving coolant supply via enhanced wicking ability. As the power consumption of electronic devices increases with their miniaturization, especially for space technologies, the development of high heat flux thermal management is crucial to effectively cool microprocessors and other high power electronics. One of the most effective solutions is to employ two-phase thermal management systems such as heat pipes and vapor chambers that allow for high heat flux cooling capability with a minimal temperature gradient.

Single-layer composite wick structures from a recent study have simultaneously achieved enhanced liquid supply and reduced thermal resistance by employing distributed wick structures[3]. In addition, a number of approaches have been tested in recent years to enhance liquid supply to the heated surface by improving wicking ability. Liu et al. have tested using a carbon fiber felt structure for the heat pipe that was chemically plated with copper, resulting in a more hydrophilic surface[4]. Nam and Ju have created cupric oxide (CuO) structures on a copper surface by chemical oxidation with various alkali solutions and thermal oxidation. These structures had the effect of significantly increasing the wetting of copper wicks[5]. Putra and Septiadi have employed tabulate coral structures which had a mean pore diameter of 52.95 μm as a wick structure to line heat pipes in a setup modeling heat transfer from a CPU. This resulted in a significant reduction of CPU temperature[6]. Feng et al. have also employed a process where they flame-sprayed a mixture of copper and aluminum onto a substrate[7]. The aluminum was then chemically leached out with sodium hydroxide, leaving behind a porous copper surface. They also created channels in the surface which further increase the permeability. They reported that an ideal capillary system would have a mix of large and small pores in order to create an optimum balance of permeability and capillary pressure.

One of the largest technical challenges for heat pipe applications is limited liquid supply to the heated surface through the thin wicks. If the liquid supplied is limited, the surface in contact with the heat source will dry out and overheat. The behavior of capillary flow through a monolayer wick should be studied in greater depth so that the flow can be optimized. This study will focus on understanding the relation between particle sizes and key transport properties such as wicking ability and permeability.

II. Experimental

A. Sample Fabrication

The samples, i.e., wicks, used in this study were manufactured using a powder sintering process[8]. To make a sample, the copper backing is first cut to size and placed into a custom stainless-steel mold. The sample length and width are 2.5 cm × 7.5 cm. The total sample thickness is 2.25 mm for single-layer samples and 2.75 mm for multi-layer samples. The mold includes a removable steel insert on the bottom which aids in sample removal after sintering and is illustrated in Figure 1. The copper powder, which is purchased from Culox Technologies Inc., is then carefully arranged on top in the desired configuration. To make a multi-layer sample, the mold is filled to the top with particles, then leveled off using a straight edge. To create the single-layer particle arrangement, the process is as follows: First, the particles are poured at one end of the rectangular sample. Then, the sample is held at a shallow angle with the particles at the higher end and gently tapped, which causes the spherical particles to roll toward the opposite end. The particles naturally arrange into a single layer as they collect on the downhill end of the sample. This process can be tedious, but with patience the results are satisfactory.

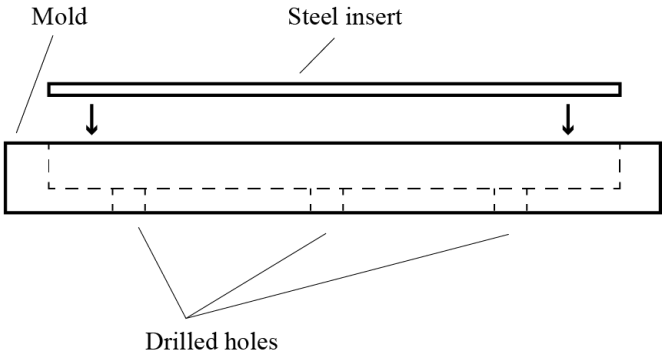

Figure 1 Side view of sample mold

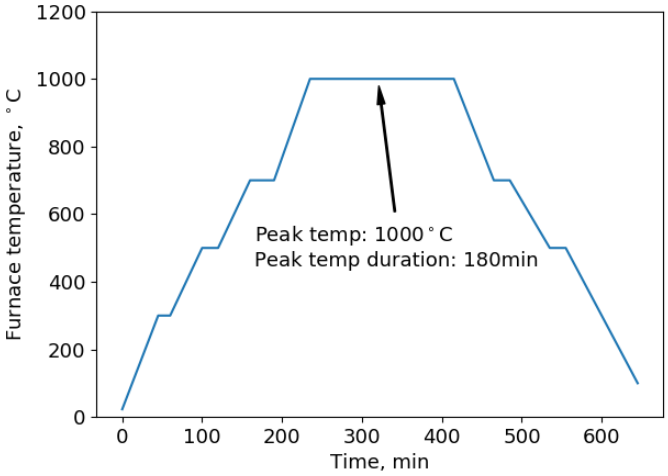

Figure 2 Temperature parameters for Sintering. *The total sintering time is 10 hours, 20 minutes including ramp-up and cool down.*

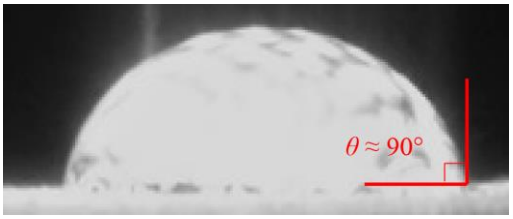

Figure 3. Contact angle between water and sintered copper particles.

Once particle arrangement is complete, the sample is put through a sintering process in a MTX OTF-1200X tube furnace. The tube furnace prevents oxidation by performing the sintering in an argon gas environment. The sample is then brought to a peak temperature of 1,000°C, is held there for 3 hr, then the temperature is slowly ramped down. The exact heating parameters are shown in Figure 2. The temperature regulation accuracy is ±1°C[9].

After sintering, the sample is de-molded by placing a small object in the holes in the rear of the mold and pressing or tapping gently on it with a hammer. The specifications of all 6 samples used in this study are listed in Table 1. For the sake of brevity, the 177 - 250 μm particle size range will be designated as 200 μm, and the 74 - 105μm range will be referred to as 100 μm. For the samples with bi-modal particle distribution (#3 and #6), a mass ratio of 75% 200 μm particles to 25% 100 μm particles was used, with the small particles evenly mixed among the large particles. Figure 4 shows optical microscope images of samples #1-3. Figure 5 illustrates the layout of the three single-layer samples.

B. Porosity Measurement

The porosity measurement method used here is similar to the one employed by Holley and Faghri[7]. Porosity is measured by comparing the masses of both dry and liquid-saturated wicks, and using the known fluid density to

Table 1. Sample Specifications including wick type, number of layers, and particle diameters.

Sample #	Wick type	# of Layers	Diameter d_{p1}, μm	Diameter d_{p2}, μm
1	Uniform (200 μm)	1	177 – 250	—
2	Uniform (100 μm)	1	74 – 105	—
3	Bi-modal (200/100 μm)	1	74 – 105	177 – 250
4	Uniform (200 μm)	5 – 8	177 – 250	—
5	Uniform (100 μm)	5 – 8	74 – 105	—
6	Bi-modal (200/100 μm)	5 – 8	74 – 105	177 – 250

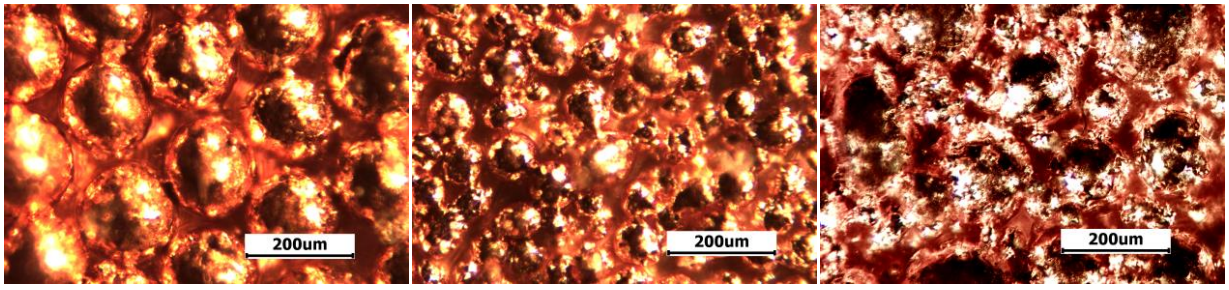

(a) Sample #1: $d_p \approx 200\mu$m **(b)** Sample #2: $d_p \approx 100\mu$m **(c)** Sample #3: $d_{p1} \approx 100\mu$m, $d_{p2} \approx 200\mu$m

Figure 4. Optical microscope images of single-layer samples #1 - #3. All images are at 100X magnification.

calculate the volume of pores and thus the porosity. Acetone was used as a working fluid due to the good wetting property. Note that water and sintered copper have a contact angle of approximately 90° as shown in Figure 4, while the contact between acetone and sintered copper is close to 0°.

The measurement procedure is as follows: A dry wick sample [Figure 6(a)] is placed on a digital mass balance, and the balanced is tared. Acetone is then added until the wick is flooded, shown in Figure 6(b). The acetone begins to evaporate, and when the wick is no longer flooded and the texture of the liquid surface is even [Figure 6(c)], the mass of the liquid saturated sample is recorded. Once the mass of liquid in the saturated wick is known, the porosity is calculated by taking the ratio between the overall volume, found by measurement with a caliper, and the volume of liquid found by the known liquid density.

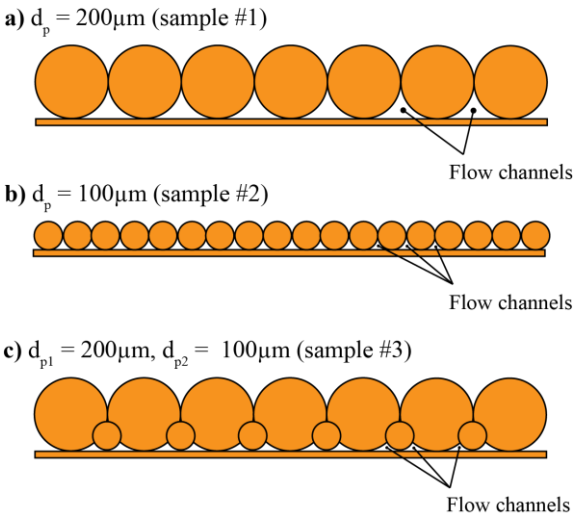

Figure 5. Layout of mono-layer samples

C. Permeability and Effective Capillary Radius Measurement

The wicking ability of the samples was measured experimentally using a custom capillary rate-of-rise test developed based on a previous study[10] as illustrated in Figure 7. It consists of a 12 in section of borosilicate glass pipe which is sealed at both ends with rubber stoppers for minimal evaporation. A small amount of working liquid is poured into the bottom of the pipe. Acetone was chosen as the working liquid due to its favorable wetting compatibility with copper and its easy availability. Only one type of working liquid was used, as previous studies have shown that changing the fluid type has little effect[10,11]. Inside the pipe is a small ruler and the sample to be tested, both held in place above the fluid using small neodemium magnets.

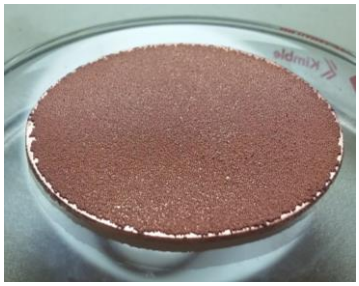

(a) Dry wick sample

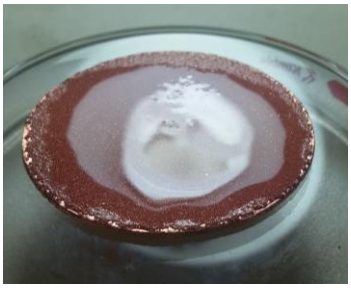

(b) Flooded wick sample

(c) Saturated wick sample

Figure 6. Sample during porosity measurement

To perform the rate-of-rise test, the sample is slowly lowered by adjusting the magnet on the exterior of the pipe until the sample contacts the fluid. The liquid then spontaneously rises into the wick due to capillary suction, shown in Figure 8. This is recorded using a video camera at 30 frames per second. After recording the first 5-10 seconds of liquid rise, the sample is left in contact with the fluid until equilibrium is reached (15-30 minutes). This final equilibrium height is recorded for the effective capillary meniscus radius r_{eff}.

To calculate r_{eff}, it is assumed that only capillary pressure and hydrostatic pressure are in effect at the equilibrium height. Equating hydrostatic pressure and a simplified Young-Laplace model for capillary pressure yields the following equations,

$$\frac{2\sigma}{r_{eff}} = \rho g h_{eq} \tag{1}$$

$$r_{eff} = \frac{2\sigma}{\rho g h_{eq}} \tag{2}$$

where ρ is liquid density, σ is surface tension, and h_{eq} liquid height at equilibrium.

To obtain the rate-of-rise plot, the video footage is split into individual frames in a video editor. Since the working liquid is transparent, it can be difficult to locate the position of the rising liquid front, but a few smoothing and contrast enhancements in an image editor increases the visibility significantly. The open source image processor ImageJ was used[12]. Once the editing is complete, the liquid height is measured frame-by-frame to obtain a plot of liquid meniscus height as a function of time. Data points for every frame are taken for the first 0.5 s and every 5 frames for the remaining time, due to the slower rate of rise after initial contact with the working liquid.

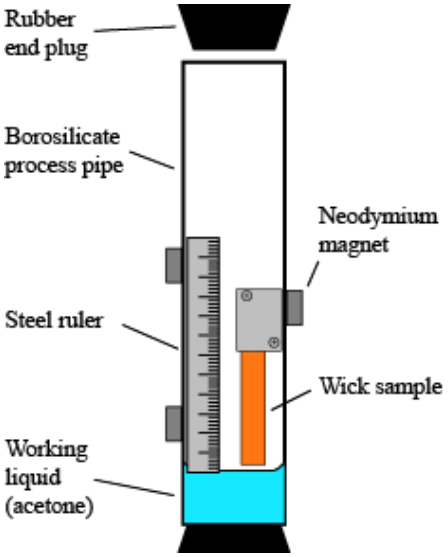

Figure 7. A schematic of rate-of-rise test setup.

The liquid rise data is then used to calculate the permeability of the sample. The calculation method uses the model implemented based on previous work[3,10]. The primary assumption in this model is that exactly three pressure differentials are in balance during the rate-of-rise test, which are capillary, viscous-frictional, and hydrostatic pressures. The Young-Laplace equation is used to formulate capillary pressure, and viscous-frictional pressure is formulated using Darcy's Law. A summation of the three pressures yields the following linear differential equation, where h is the liquid height, dh/dt is rising meniscus velocity, K is the permeability, ε is the porosity, μ is the dynamic viscosity, σ is the surface tension, r_{eff} is the effective capillary meniscus radius, ρ is the liquid density, and g is gravitational acceleration.

$$h\frac{\mathrm{d}h}{\mathrm{d}t} = \frac{K}{\varepsilon\mu}\left(\frac{2\sigma}{r_{eff}} - \rho g h\right) \tag{3}$$

Using Eq. (3), the wick particle diameter is used as an approximation of the effective capillary meniscus radius r_{eff}, as used in the previous work[10]. The following assumptions are also utilized[10]: (i) Flow is one-dimensional, steady-state, and laminar (ii) Momentum is neglected (iii) Evaporation is negligible (test is performed in a sealed tube). A curve of best fit is then found for the data using Eq. (3) using MATLAB, and the corresponding permeability is thereby obtained.

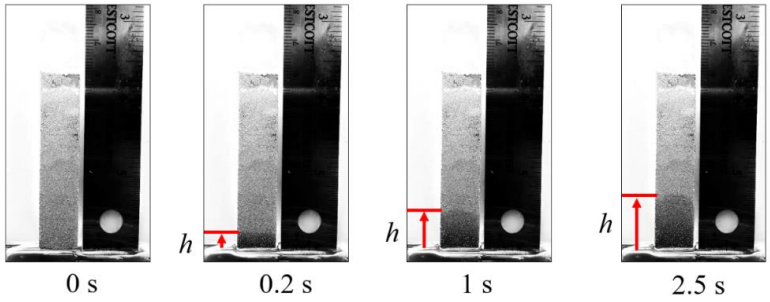

Figure 8. Snapshots of rising liquid in the wick at given elapsed time.

III. Results and Discussion

A. Porosity: Single-Layer and Multi-Layer Wicks

Table 2 shows the results of porosity measurements for all the wick types. The single-layer samples have the lowest porosity values, while the bimodal single-layer and multi-layer samples have much higher values. The 200 µm multi-layer sample has the highest measured porosity, which is nearly two-times the porosity of the single-layer samples. Although the exact origin of such a low porosity of the single layer wick, the low porosity is related to the fact that the pore size is small near the substrate due to the excessive sintering. Further study is needed to understand the reduced porosity of the single layer wick.

Table 2. Porosity Results

Sample #	Description	Porosity, ε	68.3% Confidence Interval
1	200 µm single-layer	0.25	± 0.011
2	100 µm single-layer	0.25	± 0.007
3	Bimodal single-layer	0.25	± 0.004
4	200 µm multi-layer	0.45	± 0.016
5	100 µm multi-layer	0.38	± 0.015
6	Bimodal multi-layer	0.39	± 0.021

Five trials were conducted for each sample. Based on the standard deviation for each measurement, the 68.3% confidence interval for the mean porosity was calculated for each sample and is summarized in Table 2.

B. Effect of Paticle Size d_p on Rate-of-Rise and Permeability: Single-Layer Wick

Figure 9 shows the measured liquid height change as a function of elapsed time for the single-layer wick structures, i.e., samples #1-3 (Table 1). At the beginning, the rate of rise is high, and decreases as the elapsed time increases. This is due to the increasing gravitational effect as a larger mass of liquid collects within the wick. The experimental data points scatter, which is mainly due to optically identifying the liquid front location from the images. The experimental data is curve fitted using Eq. (3) to calculate the permeability. The resulting permeability is found in Table 3.

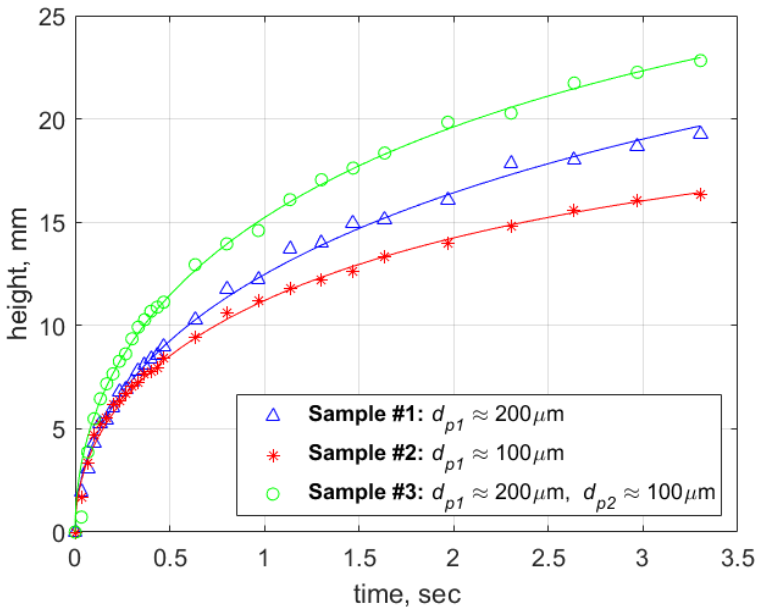

Figure 9. Rate of rise data for single-layer samples (#1-3).

As the particle diameter increases from d_p ~ 100 µm (sample #2) to d_p ~ 200 µm (sample #1), the rate-of-rise increases and the measured permebility increases by more than three times from 2.04×10^{-11} to 7.05×10^{-11}m^2. This is attributed to the fact that the larger particle sizes lead to larger effective pore sizes and permeablity. However, bi-modal size distribution 200/100 µm (sample #3) further increases the rate-of-rise and resulting permeability by nearly two times. This is related to the larger particle sizes providing the main liquid flow channels, while the smaller particle sizes decrease the effective capillary meniscus radius.

C. Effect of Paticle Size d_p on Rate-of-Rise and Permeability: Multi-Layer Wick

Figure 10 shows the measured liquid height change as a function of elapsed time for the multi-layer wick structures, i.e., samples #4-6 (Table 1). Data was taken for a shorter time range (0 to 1.5 s) compared to the single-layer wick due to difficulties in identifying the liquid height line from the images. Similar trends are observed compared to the single-layer wick structures (Figure 9), for the uniform particle-size distribution samples (#4 and #5), i.e., increasing permeability with increasing particle sizes. Comparing with the single-layer wick, the rate-of-rise and resulting permeability (Table 3) increases for all samples. This may be related to the fact that the effective capillary meniscus radius size and/or effective pore sizes are smaller than the multi-layer wick due to the flat surface from the substrate. In other words, the increased rate-of-rise of the multi-layer wick is likely due to the increased number of capillary pathways availilable within a multi-layer wick as compared to a single-layer wick. Furthur study is necessary to examine the origin of the differing rate-of-rise and permeability.

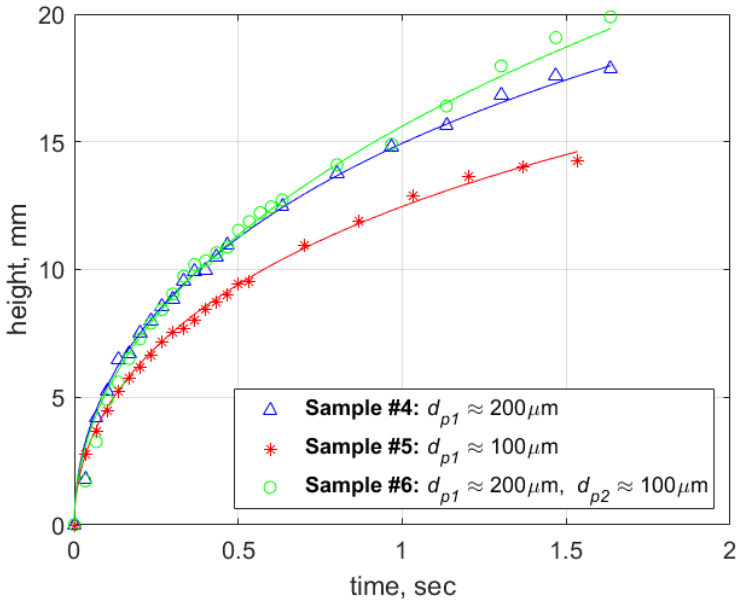

Figure 10. Rate of rise data for multi-layer samples (#4-6).

For bimodal particle-size distribution (sample #6), the rate-of-rise is enhanced compared to the single particle size wicks (#4 and #5). However, the enhancement is not as significant as compared to the effect of bimodal distribution on single-layer wicks. This marginal improvement may be related to the particle arrangement in the multi-layer wick. It was observed during manufacturing that the small 100 µm particles tended to settle in the bottom of the mold, while the large 200 µm particles stayed at the top, creating an uneven mixture. This uneven mixture may have inhibited the capillary flow pathway multiplying benefit of bimodal particle size distribution, which would have reduced the expected enhancement. Further study is planned to examine the permeability in the wick with the bimodal particle distribution.

Table 3. Permeability and r_{eff} results using Eqs. (2) and (3)

Sample #	Description	Permeability K, m^2	r_{eff}, µm
1	200 µm single-layer	7.05×10^{-11}	109-117
2	100 µm single-layer	2.04×10^{-11}	51-53
3	200/100 µm single-layer	11.66×10^{-11}	97-103
4	200 µm multi-layer	11.80×10^{-11}	—
5	100 µm multi-layer	3.040×10^{-11}	—
6	200/100 µm multi-layer	13.47×10^{-11}	—

IV. Conclusions

In this study, the permeability and wicking ability of six copper-particle-sintered wick samples were measured using the developed capillary rate-of-rise test. The wick samples were tested with varying parameters including two different particle diameters (200 µm nominal and 100 µm nominal), and two different wick thicknesses (single-layer and 5-8 layer). Samples with bi-modal particle diameters were also tested. These were a combination of 200 µm and 100µm at a 75% to 25% ratio by mass. The main conclusions are as follows:

(1) The larger particle diameter d_p increases the permeability and wicking ability.

(2) Wicks with multiple (5-8) layers increase the permeability and wicking ability as compared to single-layer wicks.

(3) Wicks with bi-modal particle size distribution have enhanced permeability and wicking ability when compared to wicks with uniform particle-size distribution.

Passive two-phase heat transfer devices such as heat pipes, heat spreaders, and loop heat pipes are heavily reliant on the wicking ablility of the interior wicks. Thus, this knowledge of the effects of wick particle-size composition on

the permeability and wicking ability will help provide pathways to improve the efficiency and utility of these critically useful devices.

Acknowledgments

This work is financially supported by NASA Cooperative Agreement Notice, Grant Number 80NSSC18M0030, and College of Engineering, Department of Mechanical Engineering, Wichita State University. Thanks to Kelvin Egbo for the contact angle picture and data. The authors thank Professor Massoud Kaviany at Department of Mechanical Engineering, University of Michigan, for the thoughtful comments into this work.

References

[1] Verdonck, J., Hugonnot, P., Ferrero, A., Martín, J. M., Serrano, M. S., and Sepúlveda, A. T., "Development and qualification of a Deployable Radiator in the frame of the European Horizon 2020 Pegasus program," p. 18.

[2] Kravets, V., Alekseik, Ye., Alekseik, O., Khairnasov, S., Baturkin, V., Ho, T., and Celotti, L., "Heat pipes with variable thermal conductance property for space applications," *Journal of Mechanical Science and Technology*, vol. 31, Jun. 2017, pp. 2613–2620.

[3] Hwang, G. S., Nam, Y., Fleming, E., Dussinger, P., Ju, Y. S., and Kaviany, M., "Multi-artery heat pipe spreader: Experiment," *International Journal of Heat and Mass Transfer*, vol. 53, 2010, pp. 2662–2669.

[4] Liu, J., Zhang, Y., Feng, C., Liu, L., and Luan, T., "Study of copper chemical-plating modified polyacrylonitrile-based carbon fiber wick applied to compact loop heat pipe," *Experimental Thermal and Fluid Science*, vol. 100, 2019, pp. 104–113.

[5] Nam, Y., and Ju, Y. S., "A comparative study of the morphology and wetting characteristics of micro/nanostructured Cu surfaces for phase change heat transfer applications," *Journal of Adhesion Science and Technology*, vol. 27, 2013, pp. 2163–2176.

[6] Putra, N., and Septiadi, W. N., "Improvement of heat pipe performance through integration of a coral biomaterial wick structure into the heat pipe of a CPU cooling system," *Heat and Mass Transfer*, vol. 53, 2017, pp. 1163–1174.

[7] Feng, C., Yugeswaran, S., and Chandra, S., "Capillary rise of liquids in thermally sprayed porous copper wicks," *Experimental Thermal and Fluid Science*, vol. 98, 2018, pp. 206–216.

[8] Nasersharifi, Y., Kaviany, M., and Hwang, G., "Pool-boiling Enhancement Using Multilevel Modulated Wick," *Applied Thermal Engineering*, vol. 137, 2018, pp. 268–276.

[9] "1200°C Split Tube Furnace with UL Recognized Components," *MTI Corp - Leading provider of lab equipments and advanced crystal substrates* Available: http://www.mtixtl.com/1200CSplitTubeFurnace-OTF-1200X-UL.aspx.

[10] Holley, B., and Faghri, A., "Permeability and effective pore radius measurements for heat pipe and fuel cell applications," *Applied Thermal Engineering*, vol. 26, 2006, pp. 448–462.

[11] Deng, D., Liang, D., Tang, Y., Peng, J., Han, X., and Pan, M., "Evaluation of capillary performance of sintered porous wicks for loop heat pipe," *Experimental Thermal and Fluid Science*, vol. 50, 2013, pp. 1–9.

[12] Schindelin, J., Arganda-Carreras, I., Frise, E., Kaynig, V., Longair, M., Pietzsch, T., Preibisch, S., Rueden, C., Saalfeld, S., and Schmid, B., "Fiji: an open-source platform for biological-image analysis," *Nature methods*, vol. 9, 2012, p. 676.